

# Chirality-Dependent Second Harmonic Generation of MoS<sub>2</sub> Nanoscroll with Enhanced Efficiency

Qingkai Qian, Rui Zu, Qingqing Ji, Gang Seob Jung, Kunyan Zhang, Ye Zhang, Markus J. Buehler, Jing Kong, Venkatraman Gopalan, and Shengxi Huang\*



Cite This: ACS Nano 2020, 14, 13333–13342



Read Online

ACCESS |

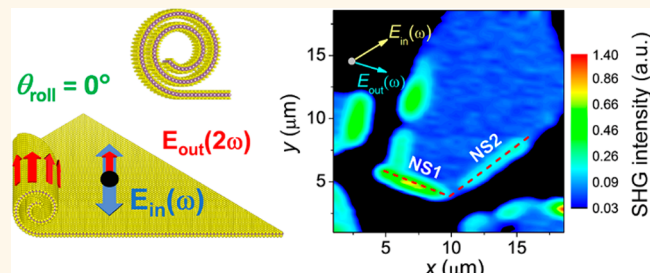
Metrics & More

Article Recommendations

Supporting Information

**ABSTRACT:** Materials with high second harmonic generation (SHG) efficiency and reduced dimensions are favorable for integrated photonics and nonlinear optical applications. Here, we fabricate MoS<sub>2</sub> nanoscrolls with different chiralities and study their SHG performances. As a 1D material, MoS<sub>2</sub> nanoscroll shows reduced symmetry and strong chirality dependency in the polarization-resolved SHG characterizations. This SHG performance can be well explained by the superposition theory of second harmonic field of the nanoscroll walls. MoS<sub>2</sub> nanoscrolls with certain chiralities and diameters in our experiment can have SHG intensity up to 95 times stronger than that of monolayer MoS<sub>2</sub>, and the full potential can still be further exploited. The same chirality-dependent SHG can be expected for nanoscrolls or nanotubes composed of other noncentrosymmetric 2D materials, such as WS<sub>2</sub>, WSe<sub>2</sub>, and hBN. The characterization and analysis results presented here can also be exploited as a nondestructive technique to determine the chiralities of these nanoscrolls and nanotubes.

**KEYWORDS:** MoS<sub>2</sub>, nanoscroll, nanotube, second harmonic generation, chirality



The development of nonlinear optics largely relies on emerging material systems that possess high nonlinear susceptibility, processability, and ease of photonic integration and device miniaturization, which has been actively pursued for decades among the optics community.<sup>1–8</sup> Second harmonic generation (SHG), as an essential nonlinear optical effect, is broadly used for applications, such as frequency conversion, light modulation, and material characterizations.<sup>9–15</sup> Yet, the required noncentrosymmetry of the host crystals greatly limits the search for SHG-bearing materials.<sup>2,6,8,11,16</sup> One recent advance that mitigates this is the rise of two-dimensional materials, such as monolayer transition metal dichalcogenides (TMDs), which generally have reduced crystal symmetries than their bulk counterparts and exhibit strong SHG signals considering their atomic thicknesses.<sup>3,4,11,17</sup> The atomic scale can also enable miniaturized device fabrication and integration. Nevertheless, the ultimately scaled thickness of such 2D materials poses a great challenge because of their insufficient light-matter interaction. Since naturally existing bulk TMDs are in the Bernal-stacking 2H phase with restored centrosymmetry and thus vanished SHG,<sup>6–8</sup> while the synthesized 3R phase still faces the problems of synthesis difficulty and phase instability,<sup>18</sup> a method capable of aligning

the constituent layers in the multilayer/bulk TMDs without symmetry restoration is highly desired to realize phase-matched SHG between each layer and thus achieve constructive interference and enhancement of the SHG intensity up to a practically functional level.

One-dimensional nanomaterials such as multiwalled nanotubes and nanoscrolls, as a nanostructure derivative of 2D materials with further reduced symmetry, represent a promising platform to engineer the interlayer interaction for desired optical and optoelectronic properties.<sup>19–26</sup> In particular, the nanoscroll structure of a TMD monolayer with a specific chirality, which is defined as the rolling angle, can be controllably fabricated and identified with focused ion beam (FIB) patterning and a simple solvent-evaporation-driven process,<sup>21,23,25</sup> which is capable of aligning the constituent

Received: June 22, 2020

Accepted: September 14, 2020

Published: September 14, 2020



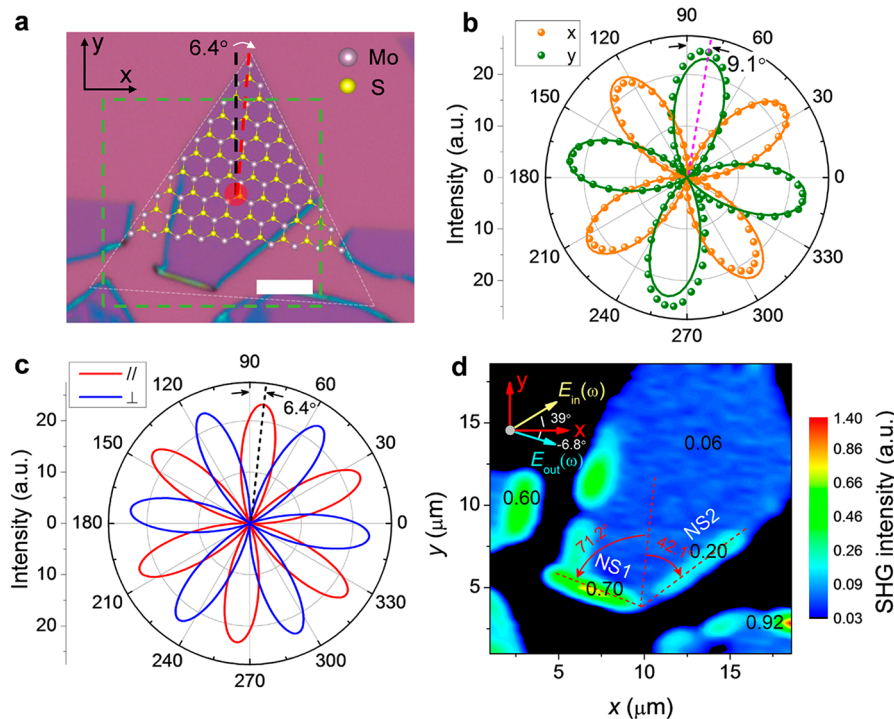


**Figure 1.** (a) Optical image of CVD-grown single-layer MoS<sub>2</sub> film and the formed nanoscrolls. Scale bar: 5  $\mu\text{m}$ . (b) Polarization-resolved second harmonic generation (SHG) of MoS<sub>2</sub> monolayer measured at the red dot position in (a) with the second harmonic (SH) electric field polarized along  $x$  and  $y$  directions. The dots are experimental results, while the solid curves are theoretical fittings. (c) Converted polarization-resolved SHG of MoS<sub>2</sub> film with SH electric field polarized along parallel and perpendicular directions of the incident laser polarization. (d) Mapping of SHG intensity of MoS<sub>2</sub> monolayer and the nanoscrolls in the green dashed square region of (a).

layers and realizing the long-pursued structural property for SHG enhancement. Moreover, the reduced dimensionality could give rise to anisotropy in the nonlinear optical response that holds promise for miniaturized polarization-dependent applications. These aspects, however, are still experimentally underexplored.

In this work, we fabricate 1D MoS<sub>2</sub> nanoscrolls out of chemical vapor deposition (CVD) MoS<sub>2</sub> monolayers, using a solvent-evaporation-driven rolling process.<sup>21,23,25</sup> We determine the nanoscroll chiralities (i.e., rolling directions) from the unscrolled triangular monolayer parts and reveal an anisotropic and chirality-dependent SHG enhancement up to 2 orders of magnitude compared with monolayer MoS<sub>2</sub>. An analytical model by considering the coherent second harmonic (SH) field superposition is established and well explains the SHG properties of the MoS<sub>2</sub> nanoscrolls. More accurate simulations including the wave propagation effect further suggest a strongly anisotropic SHG pattern of nanoscrolls and nanotubes. The work presented here could enable a different paradigm in constructing and designing miniaturized anisotropic nonlinear optical nanostructures from noncentrosymmetric 2D materials.

## RESULTS AND DISCUSSION

MoS<sub>2</sub> nanoscrolls are directly obtained by rolling MoS<sub>2</sub> flakes through a solvent-evaporation-driven process.<sup>21,23,25</sup> The triangular MoS<sub>2</sub> flakes are grown on SiO<sub>2</sub>/Si substrate by CVD, with MoO<sub>3</sub> and sulfur powders as the solid precursors. By dropping isopropyl alcohol (IPA) solution on the surface, the vaporization of IPA causes MoS<sub>2</sub> flakes to roll into quasi-1D nanoscrolls at room temperature within several minutes. Figure 1a shows a partially scrolled MoS<sub>2</sub> flake that is typically

obtained. Based on the 60° vertex angle and the sharpness of the triangle edges, this MoS<sub>2</sub> flake can be determined to be Mo-zigzag edge terminated,<sup>27</sup> and the atomic structure is schematically drawn over the flake in Figure 1a.

Polarization-resolved SHG is first measured in the planar area (Red dot in Figure 1a). The sample is excited by a Ti:Sapphire femtosecond laser system (80 fs, 80 MHz, chopped at 1 kHz) centered at 800 nm, through a 50× objective (NA = 0.75). The polarization of the incident laser is continuously tuned by a motorized half-wave plate. The resulting SHG signal is collected by the same objective and selected by a dichroic mirror. In previous polarization-resolved SHG measurements, the SHG signals of TMDs are usually measured with the analyzer polarized parallel or perpendicular to the polarization of incident laser by rotating the sample, which leads to 6-fold petals in the polarization-resolved SHG pattern.<sup>4,6,8,11,13,14</sup> However, in our experiment, considering the relatively small diameter of the quasi-1D nanoscroll, the change of laser beam position during rotating the sample may lead to a large variation of SHG intensity. Therefore, for accuracy and consistency, in all of our polarization-resolved SHG measurements, the SHG signals are collected by fixing the linear analyzer along  $x$  or  $y$  direction, while rotating the polarization of the incident laser through the motorized half-wave plate. The  $x$ - and  $y$ -polarized measurements result in 4-fold petals (Figure 1b), which is consistent with our numerical analysis (see Supporting Information section 1). After fitting the results by the solid curves in Figure 1b, polarization-resolved SHG of monolayer MoS<sub>2</sub> analyzed with parallel and perpendicular polarizations of the incident laser can be converted (see Supporting Information section 1) and is

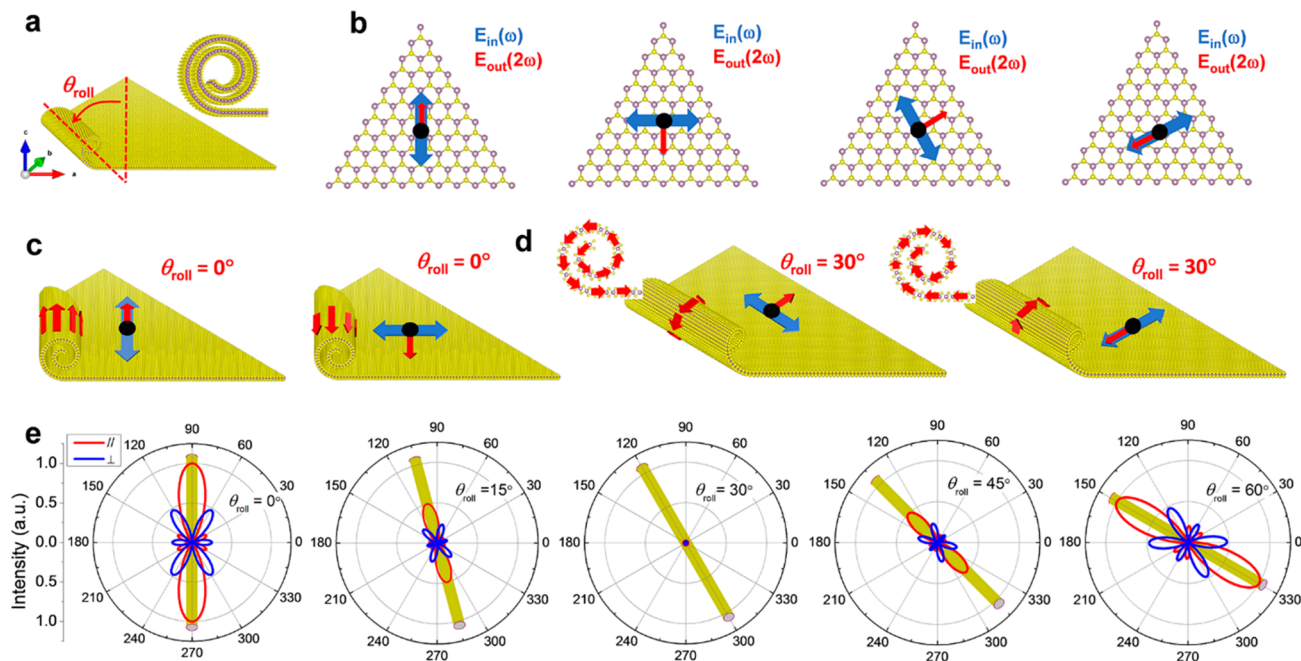


**Figure 2.** (a) Schematic of MoS<sub>2</sub> nanoscroll. (b) Electric fields (or dipoles) of the second harmonic induced by different incident laser polarizations. Schematics of second harmonic electric fields (dipoles) in a nanoscroll with (c)  $\theta_{\text{roll}} = 0^\circ$  and (d)  $\theta_{\text{roll}} = 30^\circ$  induced by incident laser polarized along and perpendicular to the nanoscroll axis, respectively. (e) Calculated polarization-resolved SHG of MoS<sub>2</sub> nanoscrolls with different chiralities.

shown in Figure 1c. The petal orientations agree with the atomic configuration in Figure 1a.

To investigate the SHG intensity of the MoS<sub>2</sub> nanoscrolls, we measure the SHG of the square region (green dashed box) in Figure 1a by scanning the sample using a piezo-driven sample stage. The mapping results are shown in Figure 1d, with the polarizations of incident laser and analyzer shown as the inset ( $E_{\text{in}}(\omega)$  and  $E_{\text{out}}(2\omega)$ ). A homogeneous SHG intensity is observed for the flat region of MoS<sub>2</sub> flake, while the nanoscrolls, such as the ones noted by NS1 and NS2 in Figure 1d, show much higher SHG intensities, which are 12 and 3.3 times larger than that of monolayer MoS<sub>2</sub> in this measurement configuration.

Figure 2a schematically draws the rolling of a nanoscroll. The rolling direction of nanoscroll  $\theta_{\text{roll}}$  is defined as the angle between the nanoscroll axis and the Mo–S bond direction (i.e., armchair direction) of the triangular flake. The enhanced SHG from the nanoscrolls is owing to the superposition of the SH electric fields from the constituent monolayer walls, which accumulate differently depending on the rolling direction, that is, the chirality of the nanoscrolls. Before touching upon this, we first consider the SHG of planar MoS<sub>2</sub> monolayer, whose SH electric field can be calculated from the second-order susceptibility tensor under the constraints of a  $P\bar{6}m2$  space group.<sup>7,16,17</sup>

$$\chi_{ijk}^{(2)} = d_0 \begin{pmatrix} 0 & (-1) & (0) \\ -1 & 0 & 0 \\ 0 & 0 & 0 \end{pmatrix} \begin{pmatrix} (-1) & (0) & (0) \\ 0 & 1 & 0 \\ 0 & 0 & 0 \end{pmatrix} \begin{pmatrix} (0) & (0) & (0) \\ 0 & 0 & 0 \\ 0 & 0 & 0 \end{pmatrix} \quad (1)$$

Here  $\chi_{ijk}^{(2)}$  is a third-order tensor,  $i$ ,  $j$ , and  $k$  are indexes that can be  $x$ ,  $y$ , or  $z$  axis,  $d_0$  is a constant related to the susceptibility amplitude of monolayer MoS<sub>2</sub>. The large parentheses in eq 1 are for  $i$ ,  $j$  indexes, while the smaller inner parentheses are for  $k$  index. To get eq 1, the armchair direction (i.e., the direction of Mo–S bonds) of triangular MoS<sub>2</sub> flake is aligned with  $y$  axis. Using this tensor, the SH electric field  $E_i^{2\omega}$  (or proportionally the generated SH polarization dipole) can be calculated by  $E_i^{2\omega} = \chi_{ijk}^{(2)} E_j^\omega E_k^\omega$ , in which  $E_j^\omega$  and  $E_k^\omega$  are the axial components of the incident laser electric field. Here the Einstein summation notation is used. For different excitation polarization, the SH electric field of a monolayer MoS<sub>2</sub> calculated using eq 1 is schematically drawn in Figure 2b. Specifically, for excitation polarized along the armchair direction of the MoS<sub>2</sub> flake, the SH electric field is along the same direction, while for excitation perpendicular to the armchair direction, that is, along the zigzag direction, the induced SH electric field is perpendicular to the incident polarization. We note that because the SH electric field  $E_i^{2\omega}$  depends on the incident electric field  $E_j^\omega$  through  $E_i^{2\omega} = \chi_{ijk}^{(2)} E_j^\omega E_k^\omega$ , it maintains the same direction for both positive and negative laser polarizations.

The second-order susceptibility tensor  $\chi_{ijk}^{(2)}$  of MoS<sub>2</sub> flake changes its mathematical form after rotation to become a part of nanoscroll walls. The mathematical transformation is provided below in eq 2.

$$\chi_{ijk}^{(2)}(R) = R_{im}\chi_{mnp}^{(2)}R_{nj}^{-1}R_{pk}^{-1} \quad (2)$$

Here  $R$  is the rotation matrix with matrix elements  $R_{ij}$ , and  $R^{-1}$  is the inverse matrix of  $R$ . The detailed derivation can be found in Supporting Information section 2. Based on the rotated tensor, SH electric fields contributed by nanoscroll walls can be calculated. Figure 2c illustrates the SH electric field distributions of a nanoscroll with  $\theta_{\text{roll}} = 0^\circ$ , with laser polarized parallel and perpendicular to the nanoscroll axis, respectively. Specifically, for incident laser parallel to the nanoscroll axis, the rolling of the MoS<sub>2</sub> flake does not change the orientation of the incident field relative to the MoS<sub>2</sub> lattice. As a result, the generated SH electric fields from different parts of the whole nanoscroll walls are still aligned in the same direction, and the total SH dipole is the simple summation of the contributions without any orientation losses, which greatly enhances the SHG efficiency. For incident laser polarized perpendicular to the nanoscroll axis, a slightly different SHG will be found, because the rolling of the MoS<sub>2</sub> flake now changes the relative direction of the incident laser polarization to the rolled MoS<sub>2</sub> lattice. For example, the electric field of the incident laser changes its sign relatively to the top and bottom parts of the nanoscroll. However, as mentioned above, the SH electric field maintains the same direction regardless of a positive or negative incident electric field. Therefore, the SH electric fields are still in-phase for enhanced emission. Nevertheless, because the incident electric field is out-of-plane for the vertical sidewalls of the nanoscroll, the overall SHG response is weaker than polarization along the nanoscroll axis. The rolling direction (i.e., chirality) of the nanoscrolls will greatly influence the SHG efficiency. Figure 2d shows the SH electric field superposition for another nanoscroll rolled along the zigzag direction ( $\theta_{\text{roll}} = 30^\circ$ ). No matter whether the excitation polarization is parallel or perpendicular to the nanoscroll axis, the SH electric field is always perpendicular to the nanoscroll axis and the SH dipole is always oriented spirally around the nanoscroll axis as indicated by the red arrows. Consequently, the total SH electric field will cancel each other, leading to a weak SHG intensity.

To analytically evaluate the chirality-dependent SHG emission of MoS<sub>2</sub> nanoscrolls, as an approximation, we calculate the effective second-order susceptibility tensor of a single-walled MoS<sub>2</sub> nanotube. This approximation ignores the continuous increase of the nanoscroll diameter, but it captures the essence of the rolled MoS<sub>2</sub> flake. On the basis of the coherent superposition theory, the effective second-order susceptibility tensor of the single-walled nanoscroll/nanotube can be calculated by summing the susceptibility tensor of the constituent walls together

$$\chi_{ijk}^{(2)}(\text{nanoscroll}) = \int_0^{2\pi} \chi_{ijk}^{(2)}(R_{\varphi,\theta_{\text{roll}},\varphi_{\text{roll}}}) d\varphi_{\text{roll}} / 2\pi \quad (3)$$

in which  $R_{\varphi,\theta_{\text{roll}},\varphi_{\text{roll}}}$  is the rotation matrix of MoS<sub>2</sub> flake from the planar orientation to a part of the nanoscroll/nanotube walls,  $\varphi$  is the rotation angle of the triangular flake from the  $y$  axis (e.g.,  $\varphi = 6.4^\circ$  in Figure 1a),  $\theta_{\text{roll}}$  is the chirality of the nanoscroll/nanotube as defined in Figure 2a,  $\varphi_{\text{roll}}$  is the rolling angle around the nanoscroll axis, which varies from 0 to  $2\pi$ , then  $\chi_{ijk}^{(2)}$

( $R_{\varphi,\theta_{\text{roll}},\varphi_{\text{roll}}}$ ) is the second-order susceptibility tensor of MoS<sub>2</sub> monolayer after rotation by  $R_{\varphi,\theta_{\text{roll}},\varphi_{\text{roll}}}$  according to eq 2. This second-order susceptibility tensor of nanoscroll is normalized by its total composed MoS<sub>2</sub> monolayer area.

On the basis of eq 3, the polarization-revolved SHG emission patterns of MoS<sub>2</sub> nanoscrolls with different chiralities are calculated in Figure 2e. Similar to monolayer MoS<sub>2</sub>, the polarization-resolved parallel and perpendicular SHG signals of nanoscrolls have six petals. Consistent with the qualitative analyses of Figure 2c and 2d, a nanoscroll with  $\theta_{\text{roll}} = 0^\circ$  has the largest SHG intensity, while nanoscroll with  $\theta_{\text{roll}} = 30^\circ$  has zero SHG intensity. Because of the 3-fold rotation symmetry of monolayer MoS<sub>2</sub> and the  $\pi$  rotation equivalence of SHG measurement, the SHG pattern of nanoscroll restores to the same SHG pattern after  $60^\circ$  rotation of  $\theta_{\text{roll}}$  only with a  $60^\circ$  global rotation.

We note that the highest SHG intensities of MoS<sub>2</sub> nanoscrolls in Figure 2e are always achieved when the laser excitation and the analyzer are both polarized along the nanoscroll axis. This can also be understood from the susceptibility tensor of nanoscroll. On the basis of eq 3, the SH susceptibility tensor for a nanoscroll/nanotube can be calculated to be

$$\chi_{ijk}^{(2)}(\text{nanoscroll}) = d_0 \cos 3\theta_{\text{roll}} \begin{pmatrix} \begin{pmatrix} 0 \\ -0.5 \\ 0 \end{pmatrix} & \begin{pmatrix} -0.5 \\ 0 \\ 0 \end{pmatrix} & \begin{pmatrix} 0 \\ 0 \\ 0 \end{pmatrix} \\ \begin{pmatrix} -0.5 \\ 0 \\ 0 \end{pmatrix} & \begin{pmatrix} 0 \\ 1 \\ 0 \end{pmatrix} & \begin{pmatrix} 0 \\ 0 \\ -0.5 \end{pmatrix} \\ \begin{pmatrix} 0 \\ 0 \\ 0 \end{pmatrix} & \begin{pmatrix} 0 \\ 0 \\ -0.5 \end{pmatrix} & \begin{pmatrix} 0 \\ 0 \\ 0 \end{pmatrix} \end{pmatrix} \quad (4)$$

in which  $\theta_{\text{roll}}$  is the roll direction defined in Figure 2a. We note that to simplify the matrix form of this tensor, the axis of the nanoscroll is selected to be  $y$  axis here (see Supporting Information section 3 for other tensor forms after rotation). From eq 4, the highest SHG intensity is caused by  $\chi_{yyy}^{(2)} = d_0 \cos 3\theta_{\text{roll}}$ . In contrast to the tensor of monolayer MoS<sub>2</sub> in eq 1, the nonzero elements of this nanoscroll tensor in the  $x-y$  plane are related by  $\chi_{xxy}^{(2)} = \chi_{xyx}^{(2)} = \chi_{yxz}^{(2)} = -\chi_{yyz}^{(2)}/2$ , instead of  $\chi_{xxy}^{(2)} = \chi_{xyx}^{(2)} = \chi_{yxz}^{(2)} = -\chi_{yyz}^{(2)}$  for the planar monolayer MoS<sub>2</sub>. The smaller ratio of  $\chi_{xxy}^{(2)}, \chi_{xyx}^{(2)}, \chi_{yxz}^{(2)}$  to  $\chi_{yyz}^{(2)}$  in the nanoscroll is caused by the out-of-plane electric field for the vertical nanoscroll sidewalls as mentioned in Figure 2c, which makes the effective exciting electric field smaller.

For the above theoretical analysis, we have assumed that the cross-section of the nanoscroll is circular. However, because of the substrate influence or the rolling dynamics, the cross-section can be elliptical (see Supporting Information section 4),<sup>23,28</sup> which will change the sidewall contributions to the SHG intensity. Using a similar calculation method as eq 3, the analytical second-order susceptibility tensor of a nanoscroll/nanotube with an elliptical cross-section can be calculated (see details in Supporting Information section 5). In our experiment, the heights and widths of the nanoscrolls are characterized by atomic force microscopy (AFM) and scanning electron microscopy (SEM). The AFM image of the fabricated

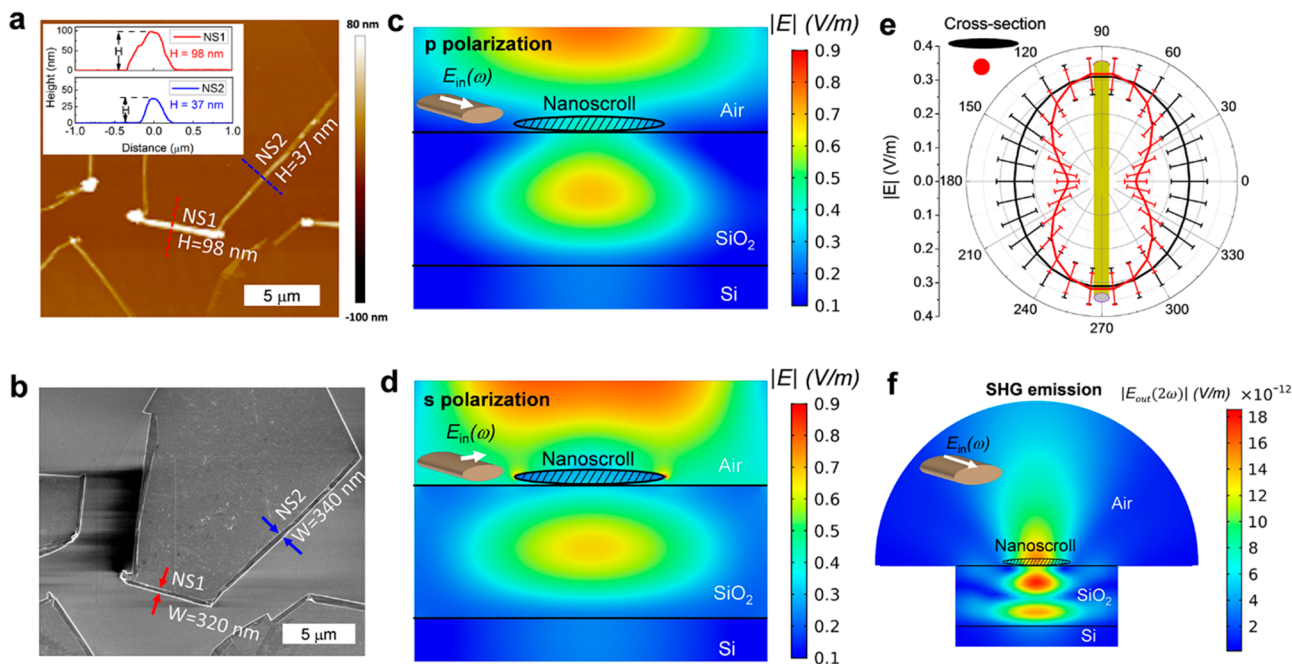


**Figure 3.** (a) AFM and (b) SEM images of the  $\text{MoS}_2$  flake and nanoscrolls. The inset of panel a shows the height profiles of selected nanoscrolls. (c, d) Simulated electric field strength of  $\text{MoS}_2$  nanoscroll on  $\text{SiO}_2/\text{Si}$  substrate with laser polarized along and perpendicular to the nanoscroll axis, respectively. (e) Polarization-resolved average electric field strength and its standard deviation inside nanoscrolls with elliptical and circular cross-sections, respectively. The nanoscroll heights are fixed at 37 nm. (f) Simulated electric field strength of the second harmonic emission.

$\text{MoS}_2$  flake and nanoscrolls is shown in Figure 3a. The cross-sectional height profiles of the selected nanoscrolls are plotted in the inset. The heights of the two nanoscrolls (NS1 and NS2) are determined to be 98 and 37 nm, respectively. Since the horizontal distances in the height profiles are influenced by the AFM tip size and the scanning speed, we use SEM to determine the widths of nanoscrolls instead. The SEM image is shown in Figure 3b, which suggests that the widths are 320 and 340 nm, respectively. According to these characterization results, we know the fabricated nanoscrolls in our experiment have oblate cross-sections with relatively large ellipticity.

The usage of one second-order susceptibility tensor to describe the SHG at different laser polarizations by  $E_i^{2\omega} = \chi_{ijk}^{(2)} E_j^\omega E_k^\omega$ , is based on the assumption that the incident electric field within the nanoscrolls/nanotubes has the same strength and phase regardless of the polarization directions. However, according to our 3D simulations using COMSOL software, the electric field strength varies significantly for different laser polarizations. Figure 3c and 3d show the simulated electric field strength of a nanoscroll with the same cross-section as NS2, with laser polarized along or perpendicular to the nanoscroll axis as schematically drawn in the insets. The nanoscroll is assumed to consist of 6 rolls, which best fit the absolute SHG intensity in the experiment. The  $\text{MoS}_2$  rolled layers are assumed to be evenly distributed within the nanoscroll that has the same cross-sectional size as that determined by our AFM and SEM measurements. The whole nanoscroll is then modeled as a solid scroll that has a volume-averaged permittivity of both  $\text{MoS}_2$  and air. Similar results can be produced if the  $\text{MoS}_2$  layers are modeled as one hollow scroll and the constituent  $\text{MoS}_2$  layers scroll compactly at the outer shell. A Gaussian beam with a full-width-at-half-maximum (fwhm) spot size of 400 nm is focused on the

substrate surface to model the laser excitation.<sup>29,30</sup> The simulation details can be found in the Methods section. The electric field strength differs between these two polarizations as shown in Figure 3c and 3d. There is a relatively stronger z-directional electric field in Figure 3d due to the light scattering at the nanoscroll vertical sidewalls when the laser is polarized perpendicular to the nanoscroll axis, making the total electric field strength less continuous at the dielectric interfaces (only  $D_z$ ,  $E_x$ , and  $E_y$  are continuous at the dielectric interfaces). Most importantly, the electric field strengths within the nanoscroll are significantly different between these two laser polarizations, which will result in distinctive SHG intensities. This polarization-dependent electric field strength for this nanoscroll is quantitatively plotted as the black curve in Figure 3e, while the red curve is the result for another nanoscroll with the same height, roll layers but a circular cross-section. The error bars show the standard deviations of the electric field strength within the nanoscrolls. With the same height, a nanoscroll with a narrower width suppresses the electric field penetration more severely when the laser is polarized perpendicular to the nanoscroll axis. In contrast, the electric field strength caused by laser polarized along the nanoscroll axis is not influenced.

Above all, two factors limit the SHG intensity when the laser is polarized perpendicular to the nanoscroll axis: first, the vertical sidewalls perceive weaker electric field strength due to the out-of-plane electric field according to the discussions of Figure 2; second, the electric field penetration and thus the absolute electric field strength are also weaker according to Figure 3. Taking both factors into account, it can be inferred that the weak side petals in Figure 2e will be further suppressed in the experiment, making the SHG pattern of the nanoscroll/nanotube more anisotropic especially when it has a circular/prolate cross-section. On the contrary, the oblate cross-sections

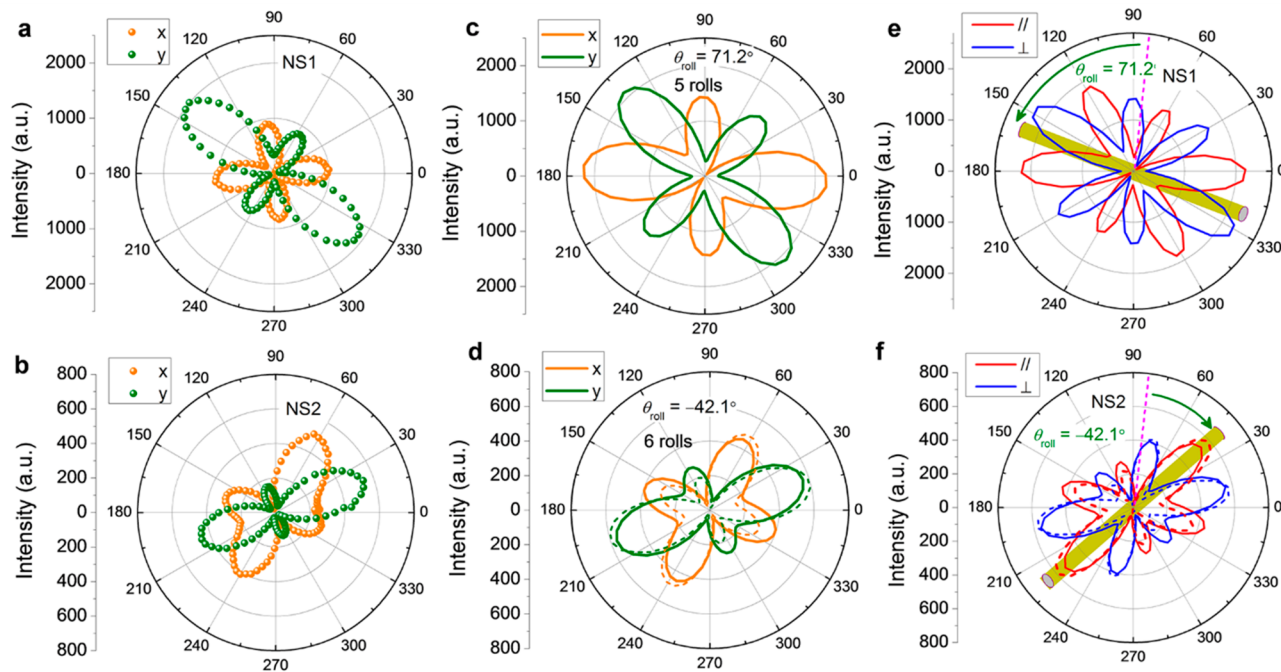


**Figure 4.** (a, b) Experimentally measured polarization-resolved SHG of two  $\text{MoS}_2$  nanoscrolls with the second harmonic electric field analyzed along  $x$  and  $y$  directions. (c, d) Simulated SHG patterns for these two nanoscrolls with elliptical cross-sections as determined by AFM and SEM. The roll numbers are tuned to best fit the measured SHG intensities. (e, f) Simulated SHG patterns with the second harmonic electric field analyzed along the parallel and perpendicular directions of incident laser polarization. The solid curves are simulation results of nanoscrolls with the constituent  $\text{MoS}_2$  layers loosely distributed in a solid scroll with a  $\text{MoS}_2$ -air volume-averaged permittivity. The dashed curves in panels d and f are simulated by a hollow scroll with a compactly scrolled  $\text{MoS}_2$  shell (18.5 nm height and 280 nm width).

of nanoscrolls in our experiment will both reduce the side-wall contributions and increase the absolute electric field strength within the nanoscrolls when the laser is polarized perpendicular to the nanoscroll axis. As a result, the anisotropy of SHG petals is reduced. Using the simulated absolute electric field strength and phase as inputs, the second harmonic polarizations of nanoscroll walls can be calculated and the SHG emission can be stimulated by a second step. A typical SHG emission pattern of the nanoscroll with laser polarized along the nanoscroll axis is shown in Figure 3f.

Figure 4a and b shows the experimentally measured polarization-resolved SHG patterns of the two nanoscrolls (NS1 and NS2) in Figure 1d, with the SH electric field analyzed along  $x$  and  $y$  directions. The SHG patterns show four petals due to this polarization configuration, similar to the case of planar  $\text{MoS}_2$  monolayer in Figure 1b. However, the absolute intensities of the four SHG petals are much larger. The highest total SHG intensities ( $I_x + I_y$ ) are obtained when the incident laser is polarized almost along the nanoscroll axis for these two nanoscrolls, which are 95 and 34 times larger than that of planar monolayer  $\text{MoS}_2$  in Figure 1b. In addition, the intensities of the four petals are not equal, indicating a symmetry breaking after scrolling. Using the obtained parameters of flake rotation angle ( $\varphi = -6.4^\circ$  in Figure 1a) and the scroll direction  $\theta_{\text{roll}}$  of the two nanoscrolls ( $71.2^\circ$  and  $-42.1^\circ$  in Figure 1d), the second harmonic emissions are simulated for different laser polarizations using COMSOL by modeling the nanoscrolls as solid scrolls with elliptical cross-sections. The simulated polarization-resolved SHG patterns are plotted in Figure 4c and d as the solid curves. SHG of monolayer  $\text{MoS}_2$  is simulated and used as an intensity calibration in these plots. The enhanced SHG intensities of

nanoscrolls are reproduced well with 5–6 rolls of  $\text{MoS}_2$  layers, consistent with the nanoscroll cross-sectional sizes and the rolled flake length ( $\sim 3\text{--}5 \mu\text{m}$ ) on the broken flake. Considering the relatively large size of the nanoscroll cross-sections, small  $\text{MoS}_2$  layer thickness (0.65 nm) and the few roll layers, the  $\text{MoS}_2$  nanoscrolls in our experiment are still rolled quite loosely. Molecular dynamics simulations and experiments suggest that the  $\text{MoS}_2$  nanoscrolls can be compactly scrolled with a much smaller circular cross-section (see Supporting Information section 4),<sup>19,25</sup> the fabrication of which will enhance the SHG efficiency to a greater extent.

The simulations show generally good agreement with the experimental results especially for nanoscroll NS2, in terms of both the polarization dependencies and relative SHG intensities. The mirror-asymmetric pattern analyzed in  $x$  direction is reproduced, which otherwise is not accounted for by a simple second-order susceptibility tensor  $\chi$ . According to the second-order susceptibility tensor, the  $x$ -polarized SHG intensity is proportional to  $\left(\frac{\chi_{xxx} + \chi_{xyy}}{2} + \chi_{xxy} \cdot \sin 2\theta + \frac{\chi_{xxx} - \chi_{xyy}}{2} \cdot \cos 2\theta\right)^2$ , which will always have a mirror symmetry (see Supporting Information section 6). The breaking of this mirror symmetry is caused by the wave propagation effect.<sup>11,29</sup> Specifically, the laser electric field at the top and bottom walls of the nanoscrolls have different phases, and there is also a phase mismatch between them during SHG emission. This phase difference and emission mismatch, in addition to the different second harmonic orientations and strengths at the top and bottom walls, lead to the fact that the total second-order emission field cannot be simply added and accurately described by a single second-order susceptibility tensor. This phase mismatch and spatial distributions of the

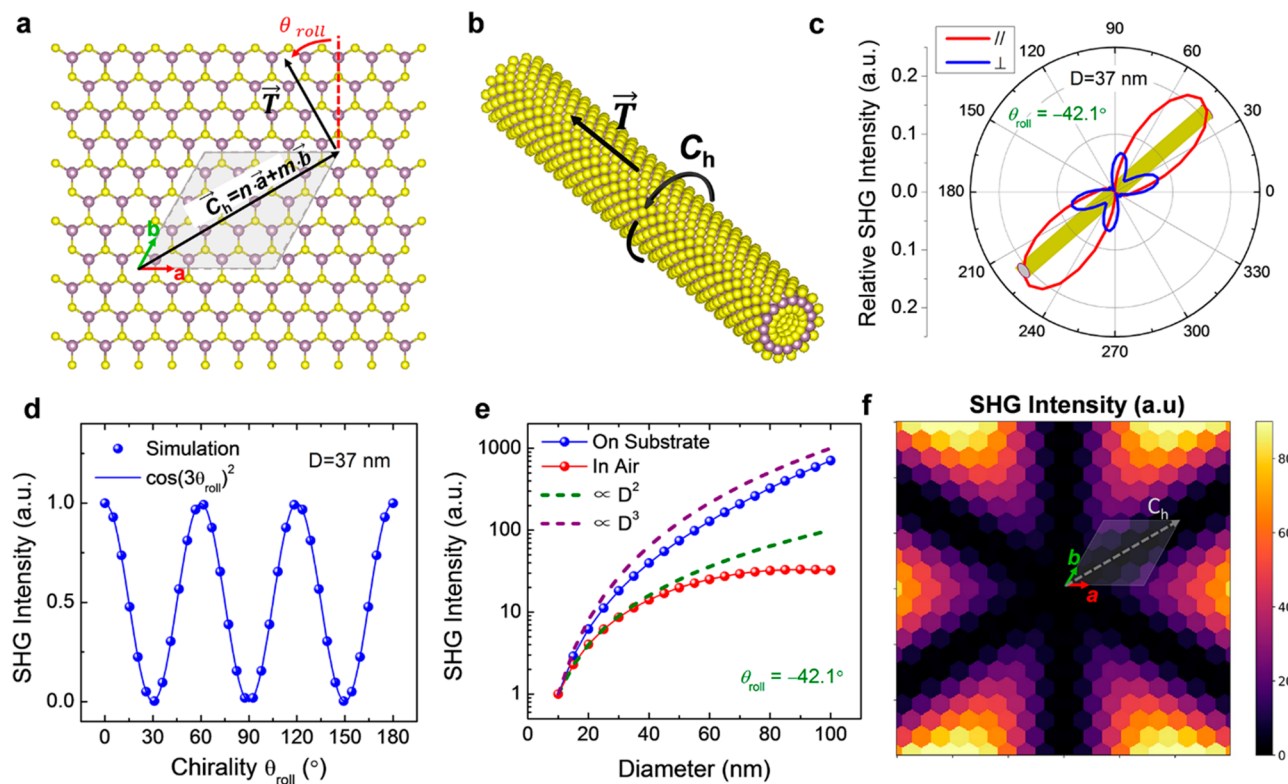


**Figure 5.** (a) Chiral vector definition of MoS<sub>2</sub> nanotube  $\vec{C}_h = n\vec{a} + m\vec{b}$ , in which  $\vec{a}$  and  $\vec{b}$  are the in-plane primitive lattice vectors of MoS<sub>2</sub>. (b) Schematic drawing of MoS<sub>2</sub> nanotube by wrapping MoS<sub>2</sub> sheet along the vector direction  $\vec{T}$ . (c) Simulated polarization-resolved SHG of a single-walled nanotube with a 37 nm diameter,  $-42.1^\circ$  roll angle and a circular cross-section. (d, e) Simulated SHG intensities of the nanotube with different chiralities and diameters. (f) SHG intensity map of MoS<sub>2</sub> nanotubes with different chiralities. Both incident laser and analyzer are polarized along the nanotube axis for panels d–f.

electric field are considered in the COMSOL simulations, and thus the mirror asymmetric SHG patterns are reproduced. On the basis of the simulations, Figure 4e and 4f plot the polarization-resolved SHG patterns simulated with parallel and perpendicular analyzers. Relatively weaker anisotropies than those in Figure 2e are observed due to the oblate cross-sections of nanoscrolls.

There are some discrepancies between the experimental results and simulations, which could be due to some unknown scrolling structures in the nanoscroll cross-sections. The discrepancies are especially large for nanoscroll NS1 when the SHG is analyzed along  $y$  axis, even though the petal orientations are still consistent. The simulated electric field strength suggests that the SHG intensity of NS1 is largely contributed by its top walls because NS1 has a relatively large diameter (98 nm) and they are closer to the standing electromagnetic wave peak induced by the incident and reflected laser. Since the second harmonic polarization is proportional to  $E_{in}(\omega)^2$ , the contribution of the top walls then becomes important. A careful check finds that this nanoscroll is closer to the MoS<sub>2</sub> triangular flake center, which may consist of growth nucleation seeds and small bilayer MoS<sub>2</sub> areas as identified by the unfolded flake areas. Since the nanoscrolls are treated as evenly distributed rolls within the cross-section in our simulations, these unknown detailed factors are not considered and might be responsible for the above discrepancies. To further verify this point, as shown by the dashed curves in Figure 4d and 4f, we conducted another COMSOL simulation, on a nanoscroll of a compactly scrolled

6-roll hollow nanoscroll with 18.5 nm height and 280 nm width that could be understood as an approximate structure of nanoscroll NS2 (37 nm height and 340 nm width with some uncertain scrolling structures). We found that this hollow nanoscroll better reproduces the experimental results of NS2, suggesting that some unknown geometric details, such as compactness of layer rolling, can affect the SHG emission patterns of nanoscrolls.

The SHG of nanoscrolls above has been simulated and well understood by the superposition of SH electric fields generated by the composed MoS<sub>2</sub> layers. Even though the experiments in this work are conducted for MoS<sub>2</sub> nanoscrolls, similar chirality-dependent SHG should be expected for MoS<sub>2</sub> nanotubes. The chirality of MoS<sub>2</sub> nanotube can be defined as Figure 5a. The  $(m, n)$  index determines the vector  $\vec{C}_h = n\vec{a} + m\vec{b}$ , which becomes the circumference of MoS<sub>2</sub> nanotube after wrapping around the axis  $\vec{T}$  as shown in Figure 5b. As an example, Figure 5c simulates the SHG emission pattern of a single-walled MoS<sub>2</sub> nanotube with a circular cross-section of 37 nm diameter and the same chirality of  $-42.1^\circ$  as NS2. Because of the inclusion of polarization-dependent electric field penetration within the nanotube by the COMSOL simulations, the simulated side petals are significantly weaker than those in Figure 2e, which even become barely visible when the laser is polarized perpendicular to the nanotube axis.

Even though eq 4 is not accurate enough to be directly used to compare the SHG intensities between different laser polarizations, for a fixed laser polarization, the analytical result can be used to distinguish the chiralities of the nanoscrolls/

nanotubes. As suggested by the COMSOL simulation in Figure 5c, for nanoscroll/nanotube with a small diameter, the SHG intensity is only significant when the laser is polarized along the nanoscroll axis. Furthermore, this parallel electric field strength is not sensitive to the cross-section of nanoscroll/nanotube as also suggested by the simulations in Figure 3e. Assuming the laser beam size is larger than the single-walled nanotube diameter  $D$ , the SHG intensity will be proportional to  $P^2 \propto D^2 \cos^2 3\theta_{\text{roll}}$  based on eq 4, in which  $P$  is the total polarization dipole of the nanotube,  $\theta_{\text{roll}}$  is the chirality as defined in Figure 2a. To verify this, we simulate the SHG intensities of single-walled nanotubes with different chiralities and diameters using COMSOL, and the results are shown in Figure 5d and 5e. The chirality dependence follows  $\cos^2 3\theta_{\text{roll}}$  very well. However, the diameter dependence follows  $D^2$  (olive dashed line) only for small-diameter nanotubes ( $<50$  nm) that are suspended in the air. For larger diameter nanotubes, the increase of SHG intensity with diameter slows down because the phase difference between the top and bottom walls of the nanotube has gradually become important and not ignorable. The overall phase mismatch can be estimated by  $(2k_\omega + k_{2\omega})D$  in our backscattering SHG scheme, in which  $k_\omega$  and  $k_{2\omega}$  are the wave vectors of incident laser and SHG light. This phase mismatch reaches approximately  $90^\circ$  for a single-walled nanotube with 50 nm diameter. For the nanotubes on the SiO<sub>2</sub>/Si substrate, the diameter dependence increases faster than  $D^2$ , because the SiO<sub>2</sub>/Si substrate can effectively reflect the laser and the larger diameter makes the nanotube closer to the standing wave peak above the substrate as shown in Figure 3c. On the basis of these discussions, Figure 5f plots the SHG intensity of suspended single-walled MoS<sub>2</sub> nanotubes with different chiralities, assuming the laser is polarized along the nanotube axes. For single-walled MoS<sub>2</sub> nanotubes on a substrate or nanotubes with large diameter ( $>50$  nm), the absolute SHG intensity needs to be further calibrated by considering the electric field strength within nanotubes due to the wave propagation and reflection. The SHG intensity map shows 6-fold symmetry, consistent with the hexagonal lattice of monolayer MoS<sub>2</sub> and the  $\pi$  rotation equivalence of SHG measurement. With a known perimeter of the nanotube, for example, obtained by AFM or SEM characterization, the chirality of MoS<sub>2</sub> nanotube can be nondestructively determined by SHG measurement using SHG intensity of the monolayer MoS<sub>2</sub> as a reference.

## CONCLUSIONS

In summary, we have fabricated MoS<sub>2</sub> nanoscrolls and characterized their polarization-resolved SHG performance. The polarization-resolved SHG can be simulated and well understood by the SH electric field superposition theory. Both the experimental results and theoretical calculations suggest that the SHG of MoS<sub>2</sub> nanoscroll has a strong chirality dependence. Besides MoS<sub>2</sub>, other noncentrosymmetric 2D materials, such as WS<sub>2</sub>, WSe<sub>2</sub>, and hBN,<sup>19,20,24,26,28,31</sup> are expected to show similar chirality-dependent SHG enhancement. In addition, our chirality-dependent SHG characterization can be further explored as a fast, convenient, and nondestructive technique to determine the chiralities of nanoscrolls and nanotubes. Compared with planar monolayer MoS<sub>2</sub> or bulk 2H-MoS<sub>2</sub>, the 1D MoS<sub>2</sub> nanoscroll can achieve much higher SHG intensity and thus emission efficiency. In our experiment, a 95X stronger SHG intensity has been achieved. Nevertheless, considering the relatively large cross-

section ( $\sim 300$  nm  $\times$  100 nm) and the small roll numbers (5–6 rolls) of the nanoscrolls in our experiment, it can be expected that by fabricating more compactly rolled nanoscrolls, even higher SHG efficiency can be achieved. Together with their reduced size and the designable anisotropic nonlinear optical responses, these nanoscrolls have advantages as functional components in integrated photonics such as a micro-sized frequency converter and optical modulator.<sup>6–8,32</sup>

## METHODS

**Sample Preparation.** The monolayer MoS<sub>2</sub> flakes were grown by the chemical vapor deposition (CVD) method on SiO<sub>2</sub>/Si substrate. MoO<sub>3</sub> and sulfur powders in two quartz boats were used as solid precursors. The grown MoS<sub>2</sub> flakes are of triangular or six-pointed star shape. To form the MoS<sub>2</sub> nanoscrolls, 100–500  $\mu$ L isopropyl alcohol (IPA) was carefully dropped on the substrate. After the solution was vaporized, the MoS<sub>2</sub> nanoscrolls were formed.

**SHG Measurement.** For the SHG measurements, the sample was excited by a Ti: Sapphire femtosecond laser system (80 fs, 80 MHz, chopped at 1 kHz) centered at 800 nm. The SHG measurement was conducted with a reflection geometry with the excitation laser normal to the sample at room temperature. The generated SHG signal was collected by a modified WITec Alpha 300 S confocal Raman microscope with a 50 $\times$  objective (NA = 0.75). The pump laser has a spot size of around 400 nm.<sup>29,30</sup> Short-pass dichroic mirror and 400 nm bandpass filter was used to ensure pure SHG signals. The SHG signals were analyzed by a linear polarizer polarized along  $x$  or  $y$  direction. To study the SHG polarimetry, the polarization of the incident laser was rotated by a motorized half-wave plate. The laser power was fixed for the SHG polarimetry for both monolayer MoS<sub>2</sub> and MoS<sub>2</sub> nanoscrolls. The SHG mapping image was taken by scanning the sample through a piezo-driven stage, with the detected SH polarization fixed at  $x$  direction and the incident laser polarization tuned to make the monolayer MoS<sub>2</sub> intensity largest.

**COMSOL Simulations.** The laser excitation and SHG emission of nanoscrolls are simulated in a 3D model using COMSOL. The necessity of using a 3D model is caused by the small laser beam size ( $\sim 400$  nm) in both parallel and perpendicular directions of the nanoscroll axis, which is smaller than the excitation laser wavelength (800 nm). Both RF and wave optics modules in COMSOL can be used, which produce the same results. The results in the manuscript are simulated using the RF module. Laser excitation is modeled by a Gaussian background beam with a fwhm of 400 nm through a top port and impedance boundary conditions are used. The nanoscrolls can be modeled as a solid or hollow scroll. The hollow scroll has the cross-sectional shape as determined in experiment by AFM and SEM and assumes the MoS<sub>2</sub> layers scroll compactly at the outer shell of the scroll. The solid scroll has also the measured cross-section of nanoscrolls, but it assumes the MoS<sub>2</sub> layers are evenly distributed within the scroll and the scroll possesses a volume-averaged permittivity of the constituent MoS<sub>2</sub> rolls and air. The second-order susceptibility tensor at different positions of the scroll is analytically calculated by the tensor rotation according to the assumed cross-sectional roll structures of MoS<sub>2</sub> layers. The tensor is input in the COMSOL model for the second-step calculation of the SHG emission. This volume second-order susceptibility tensor of the solid scroll needs to be proportionally reduced according to the air/MoS<sub>2</sub> volume ratio to maintain the total second harmonic polarization of the nanoscroll. In our simulation, the MoS<sub>2</sub> roll structures are assumed to be evenly distributed within the scroll starting from the nanoscroll center and have the same cross-sectional shape as the outer shell. Similar simulation results can be produced if the MoS<sub>2</sub> layers are modeled as one hollow scroll, and the constituent MoS<sub>2</sub> layers are scrolled compactly at the outer shell. The SHG emission is simulated in a hemisphere surrounding the nanoscroll/nanotube with the nanoscroll/nanotube at the sphere center. Only the second harmonic power flux at a part of the hemisphere surface that forms a cone is integrated as the SHG signal. The solid angle of the cone is determined by the NA (0.75) of the objective. To decompose the

electric field at the hemispherical surface into  $x$ -,  $y$ -, parallel, and perpendicular polarizations, the electric field is translated by the shortest distance through the hemispherical surface to the hemisphere apex, where  $x$ -,  $y$ -, parallel, and perpendicular polarizations are well-defined.

## ASSOCIATED CONTENT

### Supporting Information

The Supporting Information is available free of charge at <https://pubs.acs.org/doi/10.1021/acsnano.0c05189>.

Second-order susceptibility tensor of rotated MoS<sub>2</sub> flake and nanoscrolls/nanotubes; the polarization-resolved SHG pattern polarized along  $x$  and  $y$  (parallel and perpendicular) directions; and molecular dynamics simulations of compactly rolled MoS<sub>2</sub> nanoscrolls and the substrate influences ([PDF](#))

## AUTHOR INFORMATION

### Corresponding Author

**Shengxi Huang** — Department of Electrical Engineering, The Pennsylvania State University, University Park, Pennsylvania 16802, United States;  [orcid.org/0000-0002-3618-9074](https://orcid.org/0000-0002-3618-9074); Email: [sjh5899@psu.edu](mailto:sjh5899@psu.edu)

### Authors

**Qingkai Qian** — Department of Electrical Engineering, The Pennsylvania State University, University Park, Pennsylvania 16802, United States;  [orcid.org/0000-0001-7513-0676](https://orcid.org/0000-0001-7513-0676)

**Rui Zu** — Department of Materials Science and Engineering, The Pennsylvania State University, University Park, Pennsylvania 16802, United States;  [orcid.org/0000-0002-9944-4757](https://orcid.org/0000-0002-9944-4757)

**Qingqing Ji** — Department of Electrical Engineering, Massachusetts Institute of Technology, Cambridge, Massachusetts 02139, United States;  [orcid.org/0000-0001-5526-3746](https://orcid.org/0000-0001-5526-3746)

**Gang Seob Jung** — Computational Sciences and Engineering Division, Oak Ridge National Laboratory, Oak Ridge, Tennessee 37831, United States; Department of Civil and Environmental Engineering, Massachusetts Institute of Technology, Cambridge, Massachusetts 02139, United States;  [orcid.org/0000-0002-8047-6505](https://orcid.org/0000-0002-8047-6505)

**Kunyan Zhang** — Department of Electrical Engineering, The Pennsylvania State University, University Park, Pennsylvania 16802, United States;  [orcid.org/0000-0002-6830-409X](https://orcid.org/0000-0002-6830-409X)

**Ye Zhang** — Department of Electrical Engineering, Massachusetts Institute of Technology, Cambridge, Massachusetts 02139, United States; Department of Physics, Mount Holyoke College, South Hadley, Massachusetts 01075, United States

**Markus J. Buehler** — Department of Civil and Environmental Engineering, Massachusetts Institute of Technology, Cambridge, Massachusetts 02139, United States;  [orcid.org/0000-0002-4173-9659](https://orcid.org/0000-0002-4173-9659)

**Jing Kong** — Department of Electrical Engineering, Massachusetts Institute of Technology, Cambridge, Massachusetts 02139, United States;  [orcid.org/0000-0003-0551-1208](https://orcid.org/0000-0003-0551-1208)

**Venkatraman Gopalan** — Department of Materials Science and Engineering, Department of Physics, and Department of Engineering Science and Mechanics, The Pennsylvania State University, University Park, Pennsylvania 16802, United States

Complete contact information is available at:

<https://pubs.acs.org/doi/10.1021/acsnano.0c05189>

## Author Contributions

The manuscript was written through contributions of all authors. All authors have given approval to the final version of the manuscript. Q.Q. and R.Z. carried out the SHG measurements. Q.J. and Y.Z. fabricated the MoS<sub>2</sub> nanoscroll samples. Q.Q. carried out the data analysis, theoretical calculations, and COMSOL simulations of SHG. G.S.J. conducted the molecular dynamics simulations. Q.Q., K.Z., and S.H. discussed the results. The experiment was conceived and supervised by M.J.B., J.K., V.G., and S.H.

## Notes

The authors declare no competing financial interest.

## ACKNOWLEDGMENTS

R.Z. and V.G. acknowledge support from the NSF Grant DMR-1807768 and NSF-MRSEC Penn State Center for Nanoscale Science, Grant DMR-1420620. Q.J. and J.K. acknowledge the support from the STC Center for Integrated Quantum Materials with NSF Grant DMR-1231319. G.S.J. acknowledges support by the Laboratory Directed Research and Development (LDRD) Program of Oak Ridge National Laboratory and CADES for computing resources. ORNL is managed by UT-Battelle, LLC, for DOE under contract DE-AC05-00OR22725. G.S.J. and M.J.B. acknowledge support by the Office of Naval Research (Grant N00014-16-1-233 and N000141-91-2-375), ARO (Grant W911NF1920098), and DOD-MURI (Grant FA9550-15-1-0514). S.H. acknowledges the support from the National Science Foundation under grant number ECCS-1943895. COMSOL simulations for this research were performed on the Pennsylvania State University's Institute for Computational and Data Sciences Advanced CyberInfrastructure (ICDS-ACI).

## REFERENCES

- (1) Yin, X.; Ye, Z.; Chenet, D. A.; Ye, Y.; O'Brien, K.; Hone, J. C.; Zhang, X. Edge Nonlinear Optics on a MoS<sub>2</sub> Atomic Monolayer. *Science* **2014**, *344*, 488–490.
- (2) Song, Y.; Hu, S.; Lin, M.; Gan, X.; Tan, P.; Zhao, J. Extraordinary Second Harmonic Generation in ReS<sub>2</sub> Atomic Crystals. *ACS Photonics* **2018**, *5*, 3485–3491.
- (3) Autere, A.; Jussila, H.; Dai, Y.; Wang, Y.; Lipsanen, H.; Sun, Z. Nonlinear Optics with 2D Layered Materials. *Adv. Mater.* **2018**, *30*, 1705963.
- (4) Ribeiro-Soares, J.; Janisch, C.; Liu, Z.; Elias, A. L.; Dresselhaus, M. S.; Terrones, M.; Cançado, L. G.; Jorio, A. Second Harmonic Generation in WSe<sub>2</sub>. *2D Mater.* **2015**, *2*, 045015.
- (5) Kumar, N.; Najmaei, S.; Cui, Q.; Ceballos, F.; Ajayan, P. M.; Lou, J.; Zhao, H. Second Harmonic Microscopy of Monolayer MoS<sub>2</sub>. *Phys. Rev. B: Condens. Matter Mater. Phys.* **2013**, *87*, 161403R.
- (6) Shi, J.; Yu, P.; Liu, F.; He, P.; Wang, R.; Qin, L.; Zhou, J.; Li, X.; Zhou, J.; Sui, X.; Zhang, S.; Zhang, Y.; Zhang, Q.; Sun, T. C.; Qiu, X.; Liu, Z.; Liu, X. 3R MoS<sub>2</sub> with Broken Inversion Symmetry: A Promising Ultrathin Nonlinear Optical Device. *Adv. Mater.* **2017**, *29*, 1701486.
- (7) Zhao, M.; Ye, Z.; Suzuki, R.; Ye, Y.; Zhu, H.; Xiao, J.; Wang, Y.; Iwasa, Y.; Zhang, X. Atomically Phase-Matched Second-Harmonic Generation in a 2D Crystal. *Light: Sci. Appl.* **2016**, *5*, No. e16131.
- (8) Yang, D.; Hu, X.; Zhuang, M.; Ding, Y.; Zhou, S.; Li, A.; Yu, Y.; Li, H.; Luo, Z.; Gan, L.; Zhai, T. Inversion Symmetry Broken 2D 3R-MoTe<sub>2</sub>. *Adv. Funct. Mater.* **2018**, *28*, 1800785.
- (9) Carletti, L.; Locatelli, A.; Neshev, D.; De Angelis, C. Shaping the Radiation Pattern of Second-Harmonic Generation from AlGaAs Dielectric Nanoantennas. *ACS Photonics* **2016**, *3*, 1500–1507.
- (10) Marino, G.; Gigli, C.; Rocco, D.; Lemaître, A.; Favero, I.; De Angelis, C.; Leo, G. Zero-Order Second Harmonic Generation from

- AlGaAs-On-Insulator Metasurfaces. *ACS Photonics* **2019**, *6*, 1226–1231.
- (11) Li, Y.; Rao, Y.; Mak, K. F.; You, Y.; Wang, S.; Dean, C. R.; Heinz, T. F. Probing Symmetry Properties of Few-Layer MoS<sub>2</sub> and h-BN by Optical Second-Harmonic Generation. *Nano Lett.* **2013**, *13*, 3329–3333.
- (12) Shen, Y. R. Surface Properties Probed by Second-Harmonic and Sum-Frequency Generation. *Nature* **1989**, *337*, 519–525.
- (13) Hsu, W.; Zhao, Z.; Li, L.; Chen, C.; Chiu, M.; Chang, P.; Chou, Y.; Chang, W. Second Harmonic Generation from Artificially Stacked Transition Metal Dichalcogenide Twisted Bilayers. *ACS Nano* **2014**, *8*, 2951–2958.
- (14) Jiang, T.; Liu, H.; Huang, D.; Zhang, S.; Li, Y.; Gong, X.; Shen, Y.; Liu, W.; Wu, S. Valley and Band Structure Engineering of Folded MoS<sub>2</sub> Bilayers. *Nat. Nanotechnol.* **2014**, *9*, 825–829.
- (15) Kim, C.; Brown, L.; Graham, M. W.; Hovden, R.; Havener, R. W.; McEuen, P. L.; Muller, D. A.; Park, J. Stacking Order Dependent Second Harmonic Generation and Topological Defects in h-BN Bilayers. *Nano Lett.* **2013**, *13*, 5660–5665.
- (16) Shen, Y. R. *The Principles of Nonlinear Optics*; Wiley: New York, 1984.
- (17) Malard, L. M.; Alencar, T. V.; Barboza, A. P. M.; Mak, K. F.; de Paula, A. M. Observation of Intense Second Harmonic Generation from MoS<sub>2</sub> Atomic Crystals. *Phys. Rev. B: Condens. Matter Mater. Phys.* **2013**, *87*, 201401R.
- (18) Mishina, E.; Sherstyuk, N.; Lavrov, S.; Sigov, A.; Mitioglu, A.; Anghel, S.; Kulyuk, L. Observation of Two Polytypes of MoS<sub>2</sub> Ultrathin Layers Studied by Second Harmonic Generation Microscopy and Photoluminescence. *Appl. Phys. Lett.* **2015**, *106*, 131901.
- (19) Wang, W.; Gai, Y.; Xiao, D.; Zhao, Y. A Facile and General Approach for Production of Nanoscrolls with High-Yield from Two-Dimensional Nanosheets. *Sci. Rep.* **2018**, *8*, 15262.
- (20) Zhang, C.; Wang, S.; Yang, L.; Liu, Y.; Xu, T.; Ning, Z.; Zak, A.; Zhang, Z.; Tenne, R.; Chen, Q. High-Performance Photodetectors for Visible and Near-Infrared Lights Based on Individual WS<sub>2</sub> Nanotubes. *Appl. Phys. Lett.* **2012**, *100*, 243101.
- (21) Deng, W.; You, C.; Chen, X.; Wang, Y.; Li, Y.; Feng, B.; Shi, K.; Chen, Y.; Sun, L.; Zhang, Y. High-Performance Photodiode Based on Atomically Thin WSe<sub>2</sub>/MoS<sub>2</sub> Nanoscroll Integration. *Small* **2019**, *15*, 1901544.
- (22) Meng, J.; Wang, G.; Li, X.; Lu, X.; Zhang, J.; Yu, H.; Chen, W.; Du, L.; Liao, M.; Zhao, J.; Chen, P.; Zhu, J.; Bai, X.; Shi, D.; Zhang, G. Rolling up a Monolayer MoS<sub>2</sub> Sheet. *Small* **2016**, *12*, 3770–3774.
- (23) Wang, Z.; Wu, H.; Li, Q.; Besenbacher, F.; Zeng, X. C.; Dong, M. Self-Scrolling MoS<sub>2</sub> Metallic Wires. *Nanoscale* **2018**, *10*, 18178–18185.
- (24) Hwang, D. Y.; Suh, D. H. Formation of Hexagonal Boron Nitride Nanoscrolls Induced by Inclusion and Exclusion of Self-Assembling Molecules in Solution Process. *Nanoscale* **2014**, *6*, 5686–5690.
- (25) Cui, X.; Kong, Z.; Gao, E.; Huang, D.; Hao, Y.; Shen, H.; Di, C.; Xu, Z.; Zheng, J.; Zhu, D. Rolling up Transition Metal Dichalcogenide Nanoscrolls via One Drop of Ethanol. *Nat. Commun.* **2018**, *9*, 1301.
- (26) Lai, Z.; Chen, Y.; Tan, C.; Zhang, X.; Zhang, H. Self-Assembly of Two-Dimensional Nanosheets into One-Dimensional Nanostructures. *Chem.* **2016**, *1*, 59–77.
- (27) van der Zande, A. M.; Huang, P. Y.; Chenet, D. A.; Berkelbach, T. C.; You, Y.; Lee, G.; Heinz, T. F.; Reichman, D. R.; Muller, D. A.; Hone, J. C. Grains and Grain Boundaries in Highly Crystalline Monolayer Molybdenum Disulphide. *Nat. Mater.* **2013**, *12*, 554–561.
- (28) Fathipour, S.; Remskar, M.; Varlec, A.; Ajoy, A.; Yan, R.; Vishwanath, S.; Rouvimov, S.; Hwang, W. S.; Xing, H. G.; Jena, D.; Seabaugh, A. Synthesized Multiwall MoS<sub>2</sub> Nanotube and Nanoribbon Field-Effect Transistors. *Appl. Phys. Lett.* **2015**, *106*, 022114.
- (29) Denev, S. A.; Lummen, T. T. A.; Barnes, E.; Kumar, A.; Gopalan, V. Probing Ferroelectrics Using Optical Second Harmonic Generation. *J. Am. Ceram. Soc.* **2011**, *94*, 2699–2727.
- (30) Lummen, T. T. A.; Gu, Y.; Wang, J.; Lei, S.; Xue, F.; Kumar, A.; Barnes, A. T.; Barnes, E.; Denev, S.; Belianinov, A.; Holt, M.; Morozovska, A. N.; Kalinin, S. V.; Chen, L.; Gopalan, V. Thermotropic Phase Boundaries in Classic Ferroelectrics. *Nat. Commun.* **2014**, *5*, 3172.
- (31) Golberg, D.; Bando, Y.; Huang, Y.; Terao, T.; Mitome, M.; Tang, C.; Zhi, C. Boron Nitride Nanotubes and Nanosheets. *ACS Nano* **2010**, *4*, 2979–2993.
- (32) Li, D.; Wei, C.; Song, J.; Huang, X.; Wang, F.; Liu, K.; Xiong, W.; Hong, X.; Cui, B.; Feng, A.; Jiang, L.; Lu, Y. Anisotropic Enhancement of Second-Harmonic Generation in Monolayer and Bilayer MoS<sub>2</sub> by Integrating with TiO<sub>2</sub> Nanowires. *Nano Lett.* **2019**, *19*, 4195–4204.